Attracting Conductive Nonmagnetic Objects with Rotating Magnetic Dipole Fields

Devin K. Dalton¹, Griffin F. Tabor², Tucker Hermans^{2,3}, and Jake J. Abbott¹

Abstract-Recent research has shown that eddy currents induced by rotating magnetic dipole fields can produce forces and torques useful for dexterous manipulation of conductive nonmagnetic objects. This control paradigm shows promise for application in the remediation of space debris. However, the resulting force from each field source always includes a repulsive component, suggesting that the object should be surrounded by field sources to some degree to ensure the object does not leave the dexterous workspace during manipulation. In this letter, we describe the ability of multiple field sources working together in a coordinated fashion to attract conductive nonmagnetic objects that are not surrounded, reminiscent of a tractor beam. This enables an object to be pulled into a dexterous manipulation workspace. We explicitly describe the nominal attractive force on spherical objects, serving as an approximation for other object geometries, as a function of the properties of the object and the field-generation system. We perform experimental verification using a water-based microgravity simulator.

Index Terms—Space robotics and automation, manipulation planning

I. INTRODUCTION

AGNETIC manipulation has traditionally considered the manipulation of objects that comprise a large fraction of magnetic material (i.e., permanent-magnet or soft-magnetic ferromagnetic material) [1]. This limits the types of objects than can be manipulated, since many common engineering materials—including aluminum, titanium, copper, and some stainless steels—are typically considered nonmagnetic (although they may have diamagnetic or paramagnetic properties that are simply too weak to be practically useful for remote manipulation). However, these nonmagnetic materials are electrically conductive, which means that time-varying magnetic fields will induce eddy currents in them [2], which produce their own magnetic fields that interact with the applied magnetic field, which induces forces and torques on the object.

Manuscript received: Feb 24, 2022; Revised: June 10, 2022; Accepted: July 16, 2022.

This paper was recommended for publication by Editor Hyungpil Moon upon evaluation of the Associate Editor and Reviewers' comments. This work was supported by the Air Force Research Laboratory, Aerospace Systems Directorate, Rocket Propulsion Division under Educational Partnership Agreement 20-EPA-RQ-50, and by the National Science Foundation under grant number 1846341.

¹D. K. Dalton and J. J. Abbott are with the Department of Mechanical Engineering and the Robotics Center, University of Utah, Salt Lake City, UT 84112 USA. {devin.dalton, jake.abbott}@utah.edu

²G. F. Tabor and T. Hermans are with the School of Computing and the Robotics Center, University of Utah, Salt Lake City, UT 84112 USA. {griffin.tabor, tucker.hermans}@utah.edu

³T. Hermans is also with NVIDIA, Seattle, WA 98052 USA

Color versions of one or more of the figures in this letter are available online at http://ieeexplore.ieee.org.

Digital Object Identifier (DOI): see top of this page.

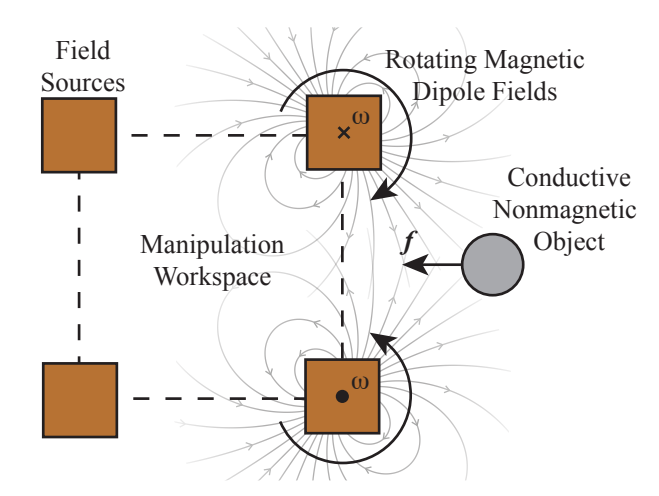


Fig. 1: Schematic depicting a conductive nonmagnetic object outside of the convex hull of a manipulation workspace being pulled into the workspace by a force f induced by multiple magnetic dipole fields rotating with frequency ω .

We recently showed that six-degree-of-freedom (6-DOF) manipulation of conductive nonmagnetic objects is possible using multiple static magnetic field sources generating rotating dipole fields about controllable axes [3]. The magnetic field sources can be electromagnets (e.g., [4]) or permanent magnets (e.g., [5,6]), although to date we have focused on the use of electromagnets. We focused our force-torque modeling and initial manipulation experiments on conductive spheres [3], which we hypothesized could serve as first-order approximations for other objects. We then actively adapted the sphere's radius based on the observed object motion to enable manipulation of unknown and non-spherical objects [7].

We are primarily interested in applications of this phenomenon in the microgravity environment of space, for which eddy-current-based actuation has received substantial attention in recent years [8–18]. The motivation for eddy current magnetic manipulation in this application is the reduction of the chance of destructive collision compared to traditional contact-based methods for the large quantities of aluminum in engineered space objects [19]. Importantly, the relatively weak induced forces and torques of the eddy currents are potentially sufficient in microgravity, as they need not overcome object weight. The induced accelerations may be small, but long time scales may be acceptable for certain applications.

In our prior modeling efforts [3,7], we found that each active field source always generates a repulsive force component, regardless of any other force and torque components, suggesting

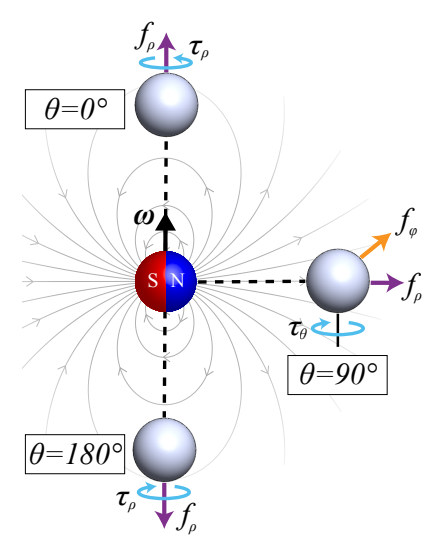


Fig. 2: Eddy-current-induced forces and torques shown in a spherical coordinate system to describe arbitrary positions of a conductive nonmagnetic object relative to a rotating magnetic dipole (with the dipole field depicted at a given instant). Note that $\hat{i}_{\phi} = \hat{i}_{\rho} \times \hat{i}_{\theta}$. The three canonical positions in [3], and their respective forces and torques, are recast in the spherical coordinate system as in [7]. The arrowhead on τ_{ρ} at $\theta = 180^{\circ}$ depicts the positive sign convention, which is opposite to the actual torque direction for the ω shown. All other force/torque arrowheads depict both the positive sign convention and the actual force/torque direction for the ω shown.

that the object must be surrounded by the field sources to some degree to effectively cage it during manipulation. We recently showed that an object can be pulled toward the nominal center of just two rotating dipole fields. In this letter we are interested in control of an object using only two rotating dipole fields. In this letter we describe and characterize the ability of multiple field sources, working together in a coordinated fashion, to attract conductive nonmagnetic objects (Fig. 1). Our method results in a capability that is reminiscent of a tractor beam—although not a tractor beam in the truest sense (i.e., a collimated beam that is able to attract one object without affecting neighboring objects)—enabling field sources to reach out and pull on objects that are not surrounded by field sources. We use dimensional analysis to characterize the method using a minimal parameterization. We explicitly consider spherical objects, as in [3].

II. REVIEW OF THE FORCE-TORQUE MODEL

In this section, we summarize our model of induced forcetorque on a solid spherical conductive object. It begins with the model from [3], which considered the object in three canonical positions relative to the rotating magnetic dipole field source. It then incorporates the extension of [7], which considers other locations of the object with respect to a rotating magnetic dipole field source, using spherical coordinates (Fig. 2).

The magnetic dipole can be abstracted as a point dipole m at position \mathcal{P}_m , rotating with angular velocity $\boldsymbol{\omega}$, such that m is orthogonal to $\boldsymbol{\omega}$. We can describe the position of the

TABLE I: Induced force and torque, and the six independent parameters that affect them, adapted from [3].

Parameter	Units	П group
\overline{f}	N	$\Pi_0 = f r^4 \mu^{-1} m^{-2}$
τ	N⋅m	$\Pi_0 = \tau r^3 \mu^{-1} m^{-2}$
σ	$A^2 \cdot s \cdot N^{-1} \cdot m^{-2} (S \cdot m^{-1})$	$\Pi_1 = \sigma \mu \omega r^2$
ρ	m	$\Pi_0 = \tau r^3 \mu^{-1} m^{-2}$ $\Pi_1 = \sigma \mu \omega r^2$ $\Pi_2 = \rho r^{-1}$
r	m	
m	A⋅m ²	
ω	s^{-1} (Hz)	
μ	$N \cdot A^{-2}$	

TABLE II: Coefficients for the models in (1) and (2) for two canonical positions, based on finite-element-analysis (FEA) simulations and experiments as reported in [3], recast in spherical coordinates as in [7].

•										
	FEA Simulations									
	θ	f, τ	Coefficients							
		,,,	c_0	c_1	c_2	<i>c</i> ₃	<i>c</i> ₄	<i>c</i> ₅		
	0_{\circ}	f_{ρ}	430	2.95	-0.101	-9.26	7	4		
	0_{\circ}	$ \tau_{\rho} $	6840	3.00	-0.0986	-13.2	6	3		
ĺ	90°	fρ	266	2.60	-0.101	-7.65	7	4		
	90°	$ \dot{f_{\phi}} $	6040	3.45	-0.102	-14.3	7	4		
	90°	$ au_{ heta}$	8100	3.60	-0.0985	-15.7	6	3		
	Experimental									
Ì	θ	f, τ	Coefficients							
		c_0	c_1	c_2	<i>c</i> ₃	<i>c</i> ₄	c_5			
	0°	f_{ρ}	467	2.81	-0.0969	-9.75	7	4		
	0°	$ \tau_{\rho} $	6900	3.35	-0.0990	-14.9	6	3		
Ì	90°	f_{ρ}	282	3.20	-0.0980	-9.41	7	4		
	90°	$\dot{f_{\phi}}$	5870	3.49	-0.0973	-14.6	7	4		
	90°	$ au_{ heta}$	8000	3.40	-0.0928	-15.0	6	3		

center of the conductive object as \mathcal{P}_o and construct a relative displacement vector $\boldsymbol{\rho} = \mathcal{P}_o - \mathcal{P}_m$. The relative position of the conductive object is described by three coordinates with respect to the rotating magnetic dipole: a distance $\boldsymbol{\rho} = \|\boldsymbol{\rho}\|$, a polar angle $\boldsymbol{\theta}$ measured from the dipole's rotation vector $\boldsymbol{\omega}$, and an azimuthal angle $\boldsymbol{\phi}$ measuring a right-handed rotation about $\boldsymbol{\omega}$. In this coordinate system, the three canonical positions are described by $\boldsymbol{\theta} = 0^{\circ}$, $\boldsymbol{\theta} = 90^{\circ}$, and $\boldsymbol{\theta} = 180^{\circ}$.

The steady-state time-averaged eddy-current-induced force f and torque τ were modeled parametrically, at the three canonical positions, as a function of the electrical conductivity σ of the conductive sphere, the distance ρ from the dipole (modeled as a point, which would be at the center of a physical source) to the center of the conductive sphere, the radius r of the conductive sphere, the magnetic dipole strength $m = \|\mathbf{m}\|$, the dipole rotation frequency $\omega = \|\boldsymbol{\omega}\|$, and the permeability of the environment μ . Using the Buckingham Π theorem, we found that each of the forces and torques could be characterized using just two independent dimensionless Π groups (see Table I).

The resulting dimensionless model took the form

$$\Pi_0 = \frac{(c_0 \Pi_1)^{c_1 \Pi_1^{c_2}} 10^{c_3}}{\Pi_2^{c_4}} \tag{1}$$

for each of the force and torque components. The coefficients for the $\theta=0^{\circ}$ and $\theta=90^{\circ}$ positions—which is all that we will need going forward, due to the symmetry of $\theta=0^{\circ}$ and

 $\theta=180^\circ$ —are provided in Table II. The model (1) is a far-field model, which underpredicts the magnitude of force and torque when $\rho<1.5r$, approximately. The model was also developed using data in the range $0\leq\Pi_1\leq20$, so extrapolation beyond this range should be done with caution. The model can also be expressed in a more intuitive form

$$f, \tau = \frac{\left(c_0 \sigma \mu_0 \omega r^2\right)^{c_1 \left(\sigma \mu_0 \omega r^2\right)^{c_2}} 10^{c_3} \left(\mu_0 m^2\right)}{\left(\frac{\rho}{r}\right)^{c_4} r^{c_5}} \tag{2}$$

where $\mu_0 = 4\pi \times 10^{-7} \text{ N} \cdot \text{A}^{-2}$ is the permeability of free space (μ_0 is the only value of μ of any practical interest).

Given the force and torque values at $\theta=0^\circ$ and $\theta=90^\circ$, we are able to construct the force and torque at other values of θ using a set of simple trigonometric functions, which embody the type of symmetries that we might expect. The equations that describe the force and torque components in spherical coordinates—at arbitrary values of ρ and θ , and not requiring ϕ due to symmetry—which call the canonical-position model (2), are as follows:

$$f_{\rho}(\rho,\theta) = -\left(\frac{f_{\rho}(\rho,90^{\circ}) - f_{\rho}(\rho,0^{\circ})}{2}\right)\cos(2\theta) + \left(\frac{f_{\rho}(\rho,90^{\circ}) + f_{\rho}(\rho,0^{\circ})}{2}\right)$$
(3)

$$f_{\theta}(\rho, \theta) \approx 0$$
 (4)

$$f_{\phi}(\rho,\theta) = f_{\phi}(\rho,90^{\circ})\sin(\theta) \tag{5}$$

$$\tau_{o}(\rho, \theta) = \tau_{o}(\rho, 0^{\circ})\cos(\theta) \tag{6}$$

$$\tau_{\theta}(\rho, \theta) = \tau_{\theta}(\rho, 90^{\circ}) \sin(\theta) \tag{7}$$

$$\tau_{\phi}(\rho,\theta) = 0 \tag{8}$$

In this letter, we will only consider the forces (3)–(5), but we have included the torques (6)–(8) to acknowledge that there may be induced torques that contribute to the object's dynamics during the attraction maneuver described herein.

III. CHARACTERIZING NOMINAL ATTRACTION OUTSIDE THE MANIPULATION WORKSPACE

When we consider a manipulation workspace in which the object is surrounded by field sources (i.e., such that it would be caged by repulsive forces), it is natural to consider the convex hull formed by the field sources. For example, consider the workspaces for four and six field sources that have been optimally distributed on the surface of a sphere (i.e., solving the Thomson problem [20]), depicted in Fig. 3. The convex hulls comprise equilateral-triangle facets formed by three field sources in a plane (different numbers of field sources can lead to different equilateral-polygon facets) and edges formed by two field sources.

Let us now turn our attention to objects that are outside of the manipulation workspace. The fundamental conjecture of this letter is that there exist locations where we can still exercise control authority to pull an object into the manipulation workspace, even though the object is not surrounded.

For facets, we will characterize the behavior along the surface normal passing through the centroid of the facet, which we will consider the nominal attraction axis of the facet. In

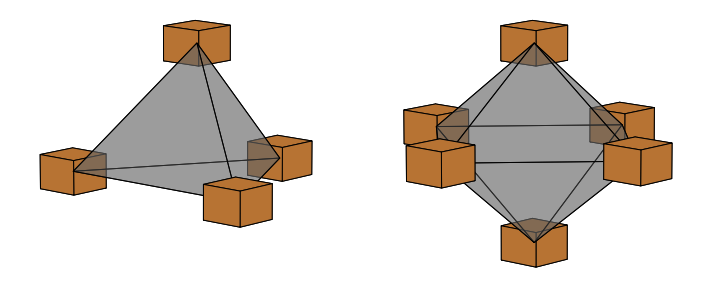


Fig. 3: Manipulation workspaces (transparent gray convex hulls) in which the object is surrounded by optimally distributed field sources (copper cubes). The convex hulls comprise edges and facets. Four field sources form a tetrahedron. Six field sources form an octahedron.

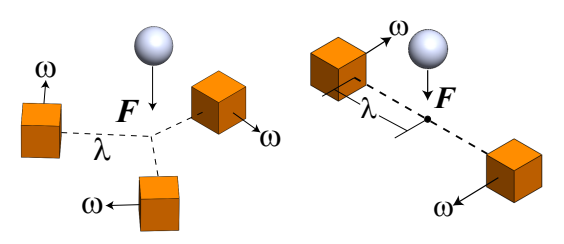


Fig. 4: Nominal attractive configurations of three field sources (without loss of generality) on a facet, and two field sources on an edge. Each field source is at a distance of λ (units m) from the nominal attraction axis. Although each field source is depicted with an ω vector, in practice we duty cycle them so that only one field source is active at any given instant.

Fig. 4(a), we depict this nominal attractive configuration of an equilateral-triangle facet. Each of the three field sources creates a rotating magnetic dipole field with an axis of rotation **ω** that is in the same plane formed by the field sources and orthogonal to the line from the centroid of the facet to the field source. Although we have explicitly described an equilateral-triangle facet comprising three field sources, we can generalize this problem formulation to equilateral-polygon facets comprising an arbitrary number of vertices (i.e., field sources).

For edges, we will characterize the nominal attraction axis of two field sources as being along any normal vector that passes through the center of the line connecting the field sources, as depicted in Fig. 4(b). Each of the two field sources creates a rotating magnetic dipole field with an axis of rotation $\boldsymbol{\omega}$ that is mutually orthogonal to both the line connecting the field sources and the normal vector.

Since our force-torque modeling of Section II does not currently allow for superposition, we will not actually actuate all N field sources simultaneously. Rather, we will duty cycle them such that they are each actuated for $1/N^{\text{th}}$ of the time. The result is that the nominal attractive capability of edges and facets comprising any number of dipole sources is the same. Consider Fig. 5, which depicts the case of two field sources (i.e., N=2), but which generalizes to all of the cases that we consider. The conductive nonmagnetic object is always at $\theta=90^\circ$ (see Fig. 2) as it moves along the normal

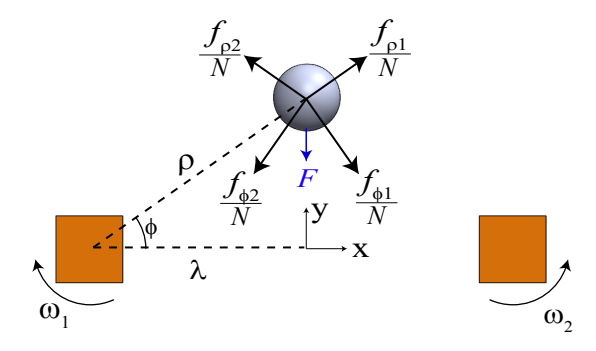


Fig. 5: Model showing the induced forces in the \hat{i}_{ρ} and \hat{i}_{ϕ} directions of the respective field source, on an object at position y on the nominal attraction axis, due to N rotating dipole fields that are each duty cycled $1/N^{\text{th}}$ of the time. The resultant pulling force F, when positive, is in the -y direction. N=2 is depicted without loss of generality

vector. Each field source generates both a radial repulsive force of magnitude $f_{\rho}=f_{\rho 1}=f_{\rho 2}$ and an orthogonal force of magnitude $f_{\phi}=f_{\phi 1}=f_{\phi 2}$, which are each scaled by N due to the duty cycle. From symmetry, force components orthogonal to the nominal attraction axis cancel, leaving only a resultant attractive force along the nominal attraction axis:

$$F = f_{\phi} \cos(\phi) - f_{\rho} \sin(\phi) \tag{9}$$

We see that the role of N has disappeared. We also note that induced torques will sum to zero.

We can form a new nondimensional dependent parameter $\Pi_0 = Fr^4\mu^{-1}m^{-2}$, analogous to how we previously nondimensionalized forces. We must also introduce a new nondimensional independent parameter to characterize attraction along the nominal axis, based on some combination of λ , ϕ , and y (given that $\Pi_2 = \rho r^{-1}$ already represents ρ in our nondimensional force model). We decided to include $\Pi_3 = y/\lambda = \tan(\phi)$, which we will show below leads to elegant results. Π_3 can take on any positive value.

When $\Pi_3 = 0$ (i.e., $\phi = 0$, on the boundary of the workspace) there will be a force equal to $f_{\phi}(\lambda, 90^{\circ})$ (see (5)) pulling the object into the workspace.

As we increase Π_3 , the resultant force will decrease and eventually transition from attraction to repulsion. This transition is defined by F = 0, which, occurs at the ϕ at which

$$\phi = \tan^{-1} \left(\frac{f_{\phi}}{f_{\rho}} \right) \tag{10}$$

with a corresponding distance

$$y_0 = \lambda \tan(\phi) = \lambda \frac{f_\phi}{f_\rho} \tag{11}$$

Attraction and repulsion occur when $y < y_0$ and $y > y_0$, respectively. Both f_{ϕ} and f_{ρ} are a function of Π_2 (i.e., a function of $\rho = \lambda/\cos(\phi) = y/\sin(\phi)$), but their ratio is not; it is only a function of Π_1 :

$$\frac{f_{\phi}}{f_{\rho}} = \frac{(c_{0\phi}\Pi_1)^{c_{1\phi}\Pi_1^{c_{2\phi}}} 10^{c_{3\phi}}}{(c_{0\alpha}\Pi_1)^{c_{1\rho}\Pi_1^{c_{2\rho}}} 10^{c_{3\rho}}}$$
(12)

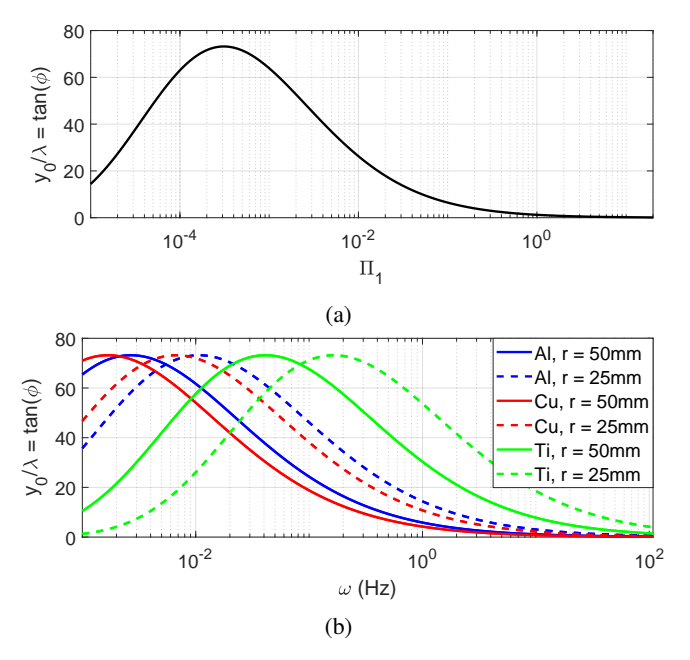


Fig. 6: Maximum normalized attraction distance Π_3 (i.e., y_0/λ) as a function of (a) Π_1 and (b) dipole rotation frequency ω for aluminum (Al), copper (Cu), and titanium (Ti) spheres of two different sizes.

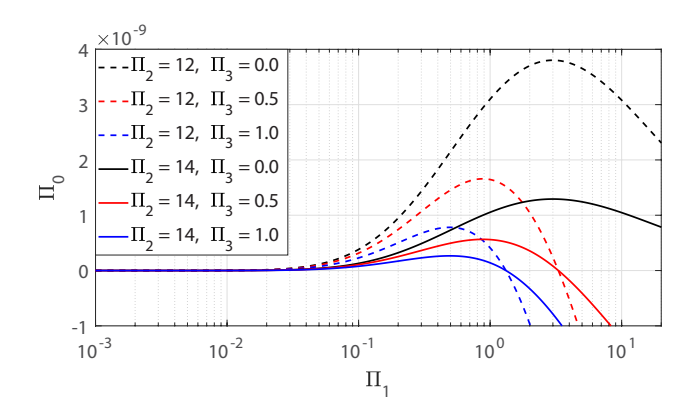


Fig. 7: Magnitude of nondimensional attractive force (Π_0) as a function of Π_1 for different combinations of Π_2 and Π_3 . A negative Π_0 indicates repulsion. Note: $\Pi_3 = 0$ corresponds to $\phi = 0^\circ$ and $\Pi_3 = 1$ corresponds to $\phi = 45^\circ$.

As a result, it is possible for us to determine the value of Π_1 —which, for a given object, is equivalent to determining the value of ω —to maximize the distance at which we can attract an object (i.e., maximize the value of Π_3 at which $\Pi_0=0$). This occurs at $\Pi_1=3\times 10^{-4}$, resulting in $y_0/\lambda=73.19$ (see Fig. 6(a)), using the "FEA Simulations" coefficients from Table II (which we use throughout this section as well as Section IV. If we look further into the construction of Π_1 (see Fig. 6(b)), we see that the optimal frequency increases as an object becomes less electrically conductive (i.e., titanium vs. copper) or smaller (r=25 mm vs. r=50 mm).

However, we have found that optimizing to maximize the distance at which we can attract objects does not lead to desirable results, since it does not account for the magnitude

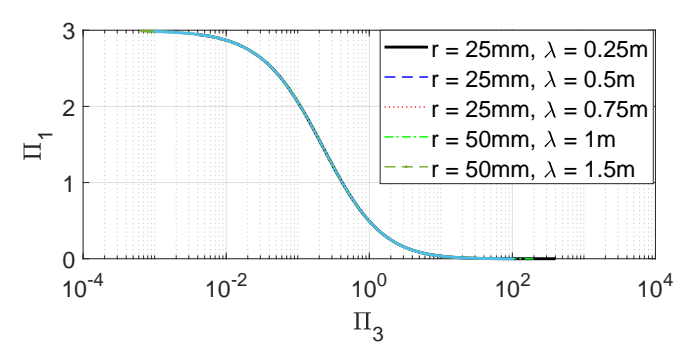


Fig. 8: The optimal Π_1 value (i.e., that maximizes attractive force) for any given Π_3 value. Multiple parameter sets are shown to demonstrate that for any given object radius or system characteristic length this relationship between the optimal Π_1 and Π_3 holds true.

of the forces that are generated, and the resulting accelerations that can be generated to pull an object into the workspace in a reasonable amount of time. Consider Fig. 7, which depicts the nondimensional magnitude of the attractive force as a function of Π_1 , at different combinations of Π_2 and Π_3 (which correspond, approximately, to values in our experiments to follow). At $\Pi_1 = 3 \times 10^{-4}$, the forces are negligible. Forces (i.e., Π_0) are maximized at Π_1 values that are orders of magnitude higher and dependent on the relative position of the object. We find that the optimal choice of Π_1 is only a function of Π_3 , although the resulting Π_0 is a function of both Π_2 and Π_3 , with increases in either leading to decreases in Π_0 as expected. Figure 8 provides the optimal value of Π_1 as a function of Π_3 : low values of Π_1 are optimal when the object is far away, and the optimal $\Pi_1 \rightarrow 3$ as the object is pulled into the workspace. It is interesting to note that [3] proposed $\Pi_1 \approx 3$ as a near-optimal value for selecting ω to use during dexterous manipulation.

For a more intuitive understanding of optimal attraction, let us consider a case study with $m=40\,\mathrm{A\cdot m^2}$, $\lambda=0.2\,\mathrm{m}$, and copper spheres (conductivity $\sigma=5.87\times10^7\,\mathrm{S\cdot m^{-1}}$, density 8960 kg·m⁻³) of two radii ($r=0.025\,\mathrm{m}$ and $r=0.05\,\mathrm{m}$). In Fig. 9(a) we show the maximum achievable attractive force F as a function of the location y on the nominal attraction axis, and in Fig. 9(b) we show the dipole frequency ω that induces it. Using these optimal forces, in Fig. 9(c) we show the amount of time it would take for the sphere, starting at rest at a given y location, to be pulled to y=0 in microgravity. We find that the optimal ω decreases with object size, and the resulting accelerations are invariant to object size.

IV. BEYOND THE NOMINAL ATTRACTION AXIS

In Section III, we explicitly considered the nominal attraction axis of facets and edges of a magnetic manipulation workspace, which exhibit a high degree of symmetry, facilitating rigorous analysis. However, we are also interested in object positions that are not on this axis of symmetry, in which we would not assume that the object would experience forces that are exclusively in the nominal attractive direction (i.e.,

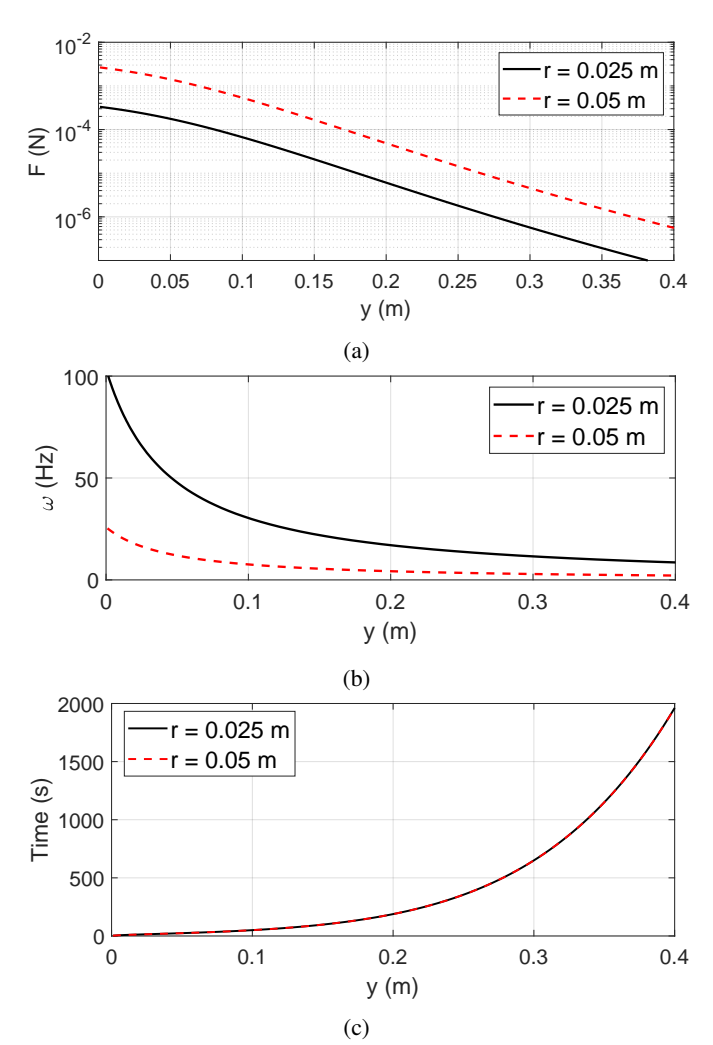


Fig. 9: (a) The maximum achievable attractive force F induced by two $m = 40 \,\mathrm{A \cdot m^2}$ rotating dipole fields with $\lambda = 0.2 \,\mathrm{m}$ on copper spheres of different radii at each location y along the nominal attraction axis, (b) the frequency ω that creates the maximum achievable attractive force, (c) and the time it takes for the sphere to be pulled to y = 0, starting at rest at each y.

the -y direction). Let us consider the (net) force vector field in the x-y plane corresponding to Fig. 5. Figure 10 shows two such force vector fields for the specific system parameters described in the preceding case study, where the value of ω is varied. As expected, the induced forces are greatest near the field sources, and they are entirely in the y direction on the nominal attraction axis (i.e., the axis of symmetry). We see that the point at which the resulting force transitions from attraction to repulsion (i.e., y_0) along the nominal attraction axis (i.e., x = 0) is a function of ω , moving toward y = 0 as ω increases, as described in Section III. There is clearly a region in which objects would be pulled between the two field sources, there are clearly regions in which objects would be pushed away, and there are regions for which an object's eventual fate is less clear.

These force vector fields are helpful visualization tools, but they do not take into account an object's inertia. This was not

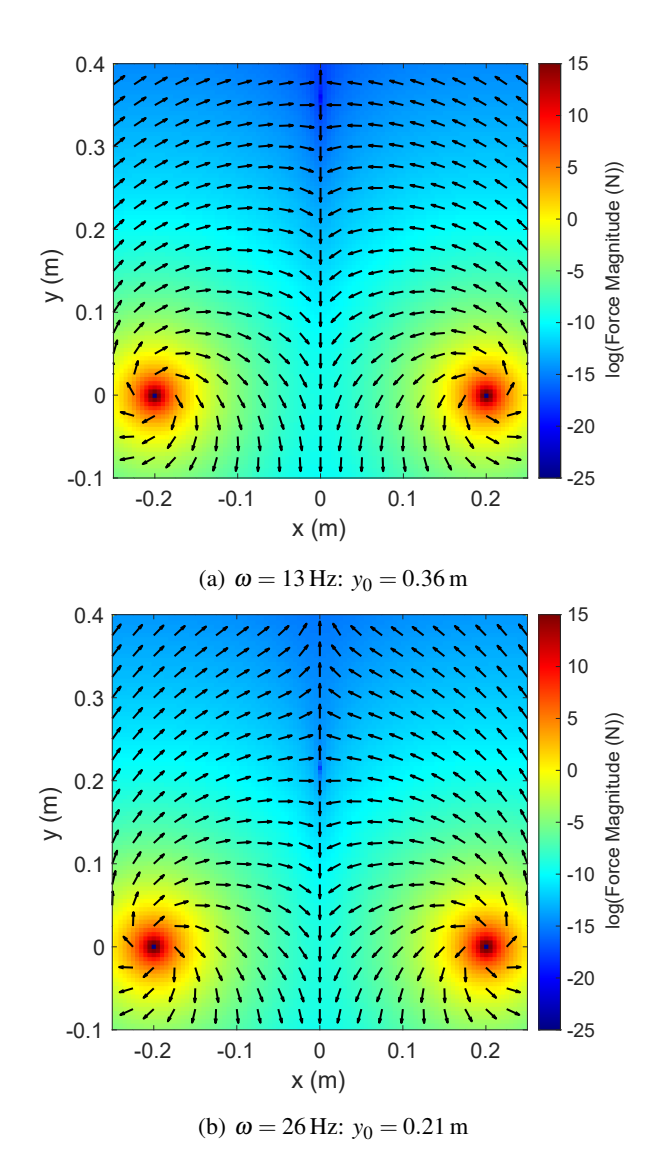


Fig. 10: Force vector field induced by two $m = 40 \,\mathrm{A \cdot m^2}$ rotating dipole fields with $\lambda = 0.2 \,\mathrm{m}$, at two frequencies, on a copper sphere with $r = 25 \,\mathrm{mm}$. See Supplemental Video 1.

a critical factor along the nominal attraction axis, since the forces always result in a straight trajectory. In order to better understand how an object within this force vector field would actually move, we created a numerical simulation that takes as inputs a spherical object's size, material properties (including density and electrical conductivity), and initial location (initial velocity was assumed to be zero), as well as the rotating dipole fields' locations, strength, and rotational frequency. The simulation outputs the resulting trajectory of the object. This simulation was then used to find the attraction/repulsion boundary for our specific system parameters. Figure 11 shows this boundary, along with some sample trajectories for various starting locations, for the same two frequencies that are shown in Fig. 10. We see a cone-shaped boundary with straight sides up to a rounded tip at y_0 . Starting within this boundary our copper sphere will be pulled between the field sources, and starting outside of this boundary our copper sphere will be pushed away. The shape of the boundary is a function of ω ,

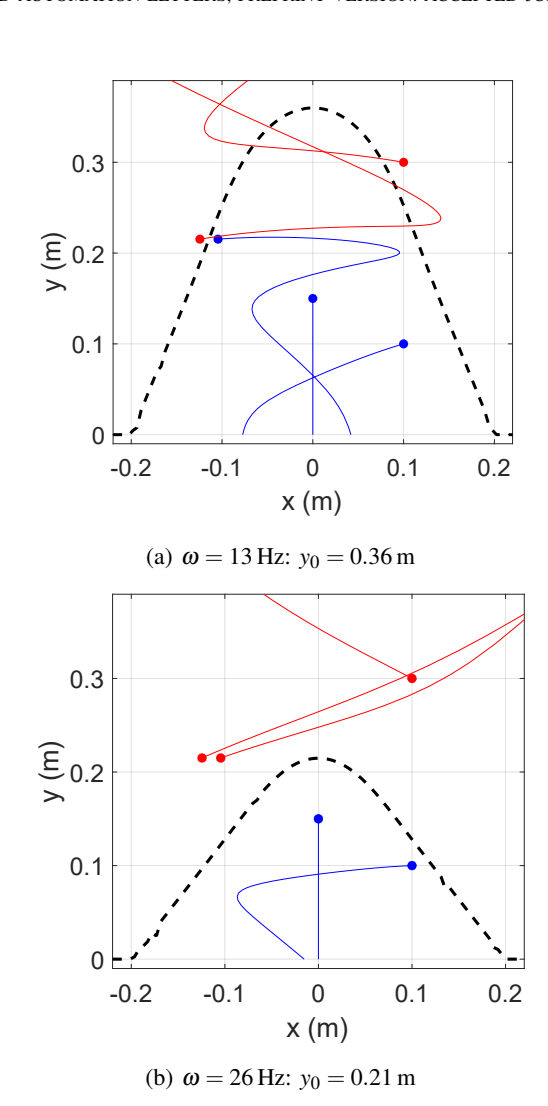
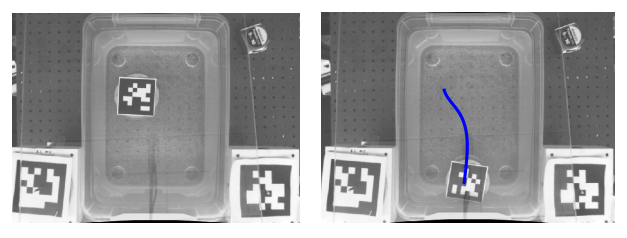


Fig. 11: Attraction/repulsion boundary and sample trajectories induced by two $m=40\,\mathrm{A\cdot m^2}$ rotating dipole fields with $\lambda=0.2\,\mathrm{m}$, at two frequencies, on a copper sphere with $r=25\,\mathrm{mm}$. The same five initial conditions are considered at both frequencies. See Supplemental Video 2.

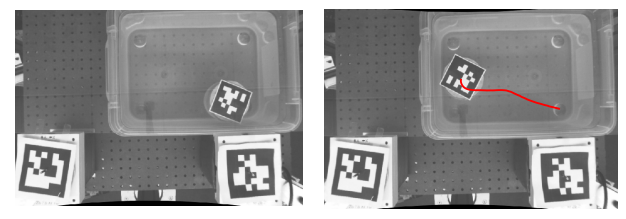
shrinking as ω increases. Both ω values in Fig. 11 consider the same five starting locations. We selected one starting location that is attractive at $\omega = 13$ Hz, but is repulsive at $\omega = 26$ Hz.

V. EXPERIMENTAL VERIFICATION

For an experimental verification of the phenomenon described above, we created an experimental setup comprising two Omnimagnets [4] of the design originally described in [21]; these are the same Omnimagnets used in our previous works on this topic [3,7]. We placed the Omnimagnets 0.4 m apart ($\lambda=0.2\,\mathrm{m}$), adjacent to a pool of water, as shown in in Fig. 12. We placed a solid copper sphere with a radius $r=0.02\,\mathrm{m}$ and mass 0.290 kg in a 3D-printed (nonmagnetic and nonconductive) raft of diameter 88 mm floating on the surface of the water, which has a depth of 100 mm. The raft itself adds another 0.055 kg to the object's mass. The pose of the raft, and thus the copper sphere, was tracked using a fiducial marker. This setup provides a 3-DOF simulation of



(a) Attraction experiment over 218 seconds.



(b) Repulsion experiment over 85 seconds.

Fig. 12: Example attraction and repulsion experiments, with initial and final conditions shown. The experimental setup comprises two Omnimagnets placed 0.4 m apart and a pool of water with a raft, equipped with a fiducial marker, carrying a 20-mm-radius copper sphere. See Supplemental Video 3. Note: the fiducial markers on the two Omnimagnets are not being utilized here.

microgravity (2-DOF translation in the horizontal plane and 1-DOF rotation about the vertical axis). The center of each Omnimagnet, which is the location of the magnetic dipole that it creates, was placed at the same vertical height as the center of the copper sphere, which is just below the surface of the water, such that experiments are conducted in the z=0 plane depicted in Fig. 5.

A frequency of $\omega = 15 \,\mathrm{Hz}$ was selected because it is the maximum frequency that we can generate while generating our maximum dipole strength of $m = 40 \,\mathrm{A \cdot m^2}$, given our system's power supply and current drives. We ran this frequency constant throughout the experiments; as a result, the results are likely suboptimal. We alternated actuating the field sources for a somewhat arbitrary duration of 2s (i.e., each with 50% duty cycle). For each experimental run we attempted to start the trajectory at rest by gently placing the raft on the water, then waiting 10 minutes to allow any ripples or starting velocities to dampen. Multiple initial positions were tested, within both the attractive and repulsive region of our system. For attraction runs, the experiment was stopped when the center of the copper sphere reached y = 0. For the repulsion runs, the experiment was stopped when the raft collided with the side of the pool. The pool was repositioned to facilitate the raft's trajectory, based on pilot runs. Two of the experimental runs are shown in Fig. 12, and four are shown in Fig. 13.

The water in our experimental environment adds both drag and additional inertia that would not be present in microgravity. To estimate these effects, we conducted an additional study in which we replaced the copper sphere with a permanent magnet with its dipole pointed downward and additional small plastic beads to match the mass of the copper sphere. We then commanded one Omnimagnet to have a constant dipole

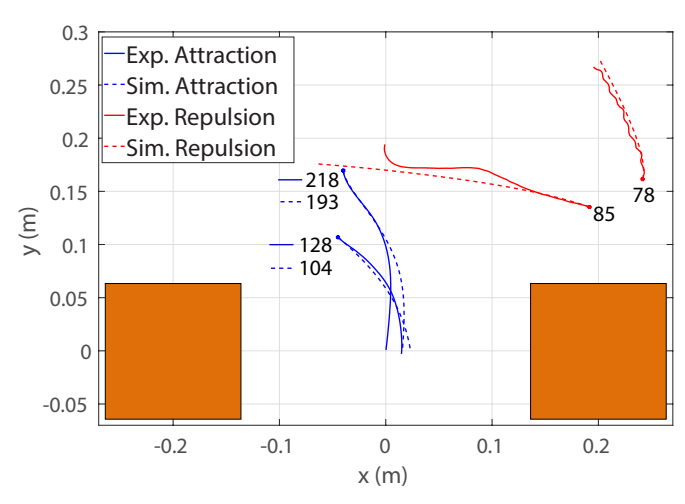


Fig. 13: Experimental and simulated trajectories. Initial positions are shown as dots. The Omnimagnets are depicted as copper squares. For the attraction experiments, the time (in seconds) to reach y = 0 is indicated. For the repulsion experiments, the simulation was run for the same amount of time as the respective experiment, which is indicated.

pointed upward that resulted in a purely attractive force on the permanent magnet [1], causing the raft to attract along a straight line. We tuned the strength of the Omnimagnet's dipole such that the raft moved with velocities comparable to our experiments described above. We used linear regression to fit an effective inertia, as well as a damping coefficient on velocity entering both linearly and quadratically; we found a significantly better fit using quadratic velocity, which is expected since the Reynolds number of our experiments is still relatively high, even at our slow velocities. The resulting best-fit model was $0.61\dot{v} + 5.4v^2 = f$. The effective mass of $0.61 \, \mathrm{kg}$, compared to the measure raft-sphere mass of $0.345 \, \mathrm{kg}$, indicates that the inertia of water is not negligible; neither is the hydrodynamic drag. This lumped model of the inertial effects of water is, of course, only a coarse approximation.

Using the above model, we simulated what we would anticipate compared to our experimental results, starting from the same initial conditions. We used the "Experimental" coefficients from Table II. The results are included in Fig. 13. We see that our model-based results are qualitatively and quantitatively similar to what we observed experimentally, with our experimental attraction runs take just 13% to 23% longer than what we anticipated from our model.

If we use a true numerical simulation of microgravity that ignores drag and inertial effects of water (as well as the added mass of a raft), starting with the same initial conditions in Fig. 13, the trajectories are qualitatively similar to the results in Fig. 13, but the velocities and accelerations are increased. The time to reach y=0 for the simulated attractive run than took 104s in water would be expected to take only 66s in microgravity. The simulated attractive run that took 193s in water would be expected to take only 128s in microgravity. For each of the repulsive runs, the object would be expected to travel farther in the same amount of time without the water. These results suggest that, although our water-based

experiment does add some parasitic effects, it is still good at approximating microgravity, as results are on the same order of magnitude as what would be expected in microgravity.

VI. DISCUSSION

Our nondimensional study considered each of the independent variables that affect our ability to attract an object using the proposed physics. However, the electromagnets' dipole strength m was selected as one of those parameters, and it must be generated using electrical power (which, fortunately, is a renewable resource for applications in space). For a given electromagnet, the dipole strength is linearly proportional to the current i (i.e., $m \propto i$) [1], and the consumed power P is quadratic with respect to current (i.e., $P = i^2 R$ for coil resistance R). Therefore, the power is quadratic with respect to the dipole strength (i.e., $P \propto m^2$). Finally, since induced forces are quadratic with respect to dipole strength (i.e., $f \propto m^2$, see (2)), we can conclude that the induced forces are linear with respect to power (i.e., $f \propto P$). The design of the electromagnets and their associated power system will be a complex design problem with many competing factors, which is beyond the scope of this letter. However, for Omnimagnets in particular, [4] provides a set of design equations that can be incorporated into such designs and feasibility studies.

Constructing the attraction/repulsion boundaries in Fig. 11 required exhaustive dynamic simulations. The result was a straight-sided, rounded-tip cone with its tip at the position $(0,y_0)$. One could simply assume a straight-sided, pointed-tip cone with its tip at the position $(0,y_0)$ to provide a conservative attraction boundary, in the sense that certain locations that are actually attractive would be considered repulsive, which does not require any simulations.

As in our prior works, we limited our analysis to solid spherical conductive nonmagnetic objects, serving as a first-order approximation for other geometries. Future studies should consider thin-walled objects, which are likely more applicable for space debris, and which we hypothesize will have more favorable acceleration properties, with a reduction in eddy-current-induced forces that is more than offset by the reduction in mass.

VII. CONCLUSION

We have demonstrated that rotating magnetic dipole fields, working together in a coordinated fashion, are capable of attracting (i.e., pulling on) conductive nonmagnetic objects in spite of the fact that each field source always induces a repulsive force component. This was accomplished by using our previously created model of eddy-current-induced force on conductive nonmagnetic spheres. We analyzed this attraction capability using an arbitrary number of field sources that are equally spaced in a plane around an axis of symmetry, which we consider the nominal attraction axis, and we determined the optimal dipole rotation frequency for a given position of the object along this axis. We also considered the behavior of objects that are not on the axis of symmetry, and determined that there are regions in which objects are eventually either

pulled between the field sources or pushed away. Through experiments with two electromagnetic field sources and a waterbased microgravity simulator, we verified that our model-based results are a good prediction of what is observed in practice.

ACKNOWLEDGMENT

The authors thank Travis Allen and Dr. Henry Fu for their contributions toward our experiments.

REFERENCES

- J. J. Abbott, E. Diller, and A. J. Petruska, "Magnetic methods in robotics," Annu. Rev. Control Robot. Auton. Syst., vol. 3, pp. 57–90, 2020
- [2] H. Hertz, Miscellaneous papers. London: Macmillan, 1896, ch. II. On induction in rotating spheres, english translation by D. E. Jones and G. A. Schott
- [3] L. N. Pham, G. F. Tabor, A. Pourkand, J. L. B. Aman, T. Hermans, and J. J. Abbott, "Dexterous magnetic manipulation of conductive nonmagnetic objects," *Nature*, vol. 598, pp. 439–443, 2021.
- [4] A. J. Petruska and J. J. Abbott, "Omnimagnet: An omnidirectional electromagnet for controlled dipole-field generation," *IEEE Trans. Magn.*, vol. 50, no. 7, p. 8400810, 2014.
- [5] A. W. Mahoney and J. J. Abbott, "Generating rotating magnetic fields with a single permanent magnet for propulsion of untethered magnetic devices in a lumen," *IEEE Trans. Robot*, vol. 30, no. 2, pp. 411–420, 2014.
- [6] S. E. Wright, A. W. Mahoney, K. M. Popek, and J. J. Abbott, "The spherical-actuator-magnet manipulator: A permanent-magnet robotic end-effector," *IEEE Trans. Robot.*, vol. 33, no. 5, pp. 1013–1024, 2017.
- [7] G. F. Tabor, L. N. Pham, J. J. Abbott, and T. Hermans, "Adaptive manipulation of conductive, nonmagnetic objects via a continuous model of magnetically induced force and torque," in *Proc. Robotics: Science* and Systems, 2022.
- [8] B. Z. Reinhardt and M. A. Peck, "New electromagnetic actuator for on-orbit inspection," *J. Spacecraft Rockets*, vol. 53, no. 2, pp. 241–248, 2016.
- [9] J.-C. Liou and N. L. Johnson, "Risks in space from orbiting debris," Science, vol. 311, pp. 340–341, 2016.
- [10] M. Shan, J. Guo, and E. Gill, "Review and comparison of active space debris capturing and removal methods," *Prog. Aerosp. Sci.*, vol. 80, pp. 18–32, 2016.
- [11] C. P. Mark and S. Kamath, "Review of active space debris removal methods," *Space Policy*, vol. 47, pp. 194–206, 2019.
- [12] National Aeronautics and Space Administration, "Astromaterials Research & Exploration Science: Orbital Debris Program Office," https://orbitaldebris.jsc.nasa.gov/, accessed: 2021-07-08.
- [13] N. Ortiz Gómez and S. J. I. Walker, "Eddy currents applied to detumbling of space debris: Analysis and validation of approximate proposed methods," *Acta Astronaut.*, vol. 114, pp. 34–53, 2015.
- [14] F. Sugai, S. Abiko, T. Tsujita, X. Jiang, and M. Uchiyama, "Detumbling an uncontrolled satellite with contactless force by using an eddy current brake," in *Proc. IEEE/RSJ Int. Conf. Intelligent Robots and Systems*, 2013, pp. 783–788.
- [15] X. Liu, Y. Lu, Q. Zhang, and K. Zhang, "An application of eddy current effect on the active detumble of uncontrolled satellite with tilt air gap," *IEEE Trans. Magn.*, vol. 55, no. 12, pp. 1–11, 2019.
- [16] M. A. Nurge, R. C. Youngquist, and S. O. Starr, "Drag and lift forces between a rotating conductive sphere and a cylindrical magnet," Am. J. Phys., vol. 86, no. 6, pp. 443–452, 2018.
- [17] K. T. Wilson and M. A. Peck, "Electromagnetic actuation for non-contact, propellant-free, six-degree-of-freedom relative mobility," in Proc. AIAA Scitech Forum, no. 2021-0074, 2021.
- [18] K. T. Wilson, G. Bernal, and M. A. Peck, "A translating eddy-current actuator for relative positioning of spacecraft," in *Proc. AIAA Scitech Forum*, no. 2022-2386, 2022.
- [19] J. N. Opiela, "A study of the material density distribution of space debris," Adv. Space Res., vol. 43, no. 7, pp. 1058–1064, 2009.
- [20] J. J. Thomson, "The structure of the atom: an investigation of the stability and periods of oscillation of a number of corpuscles arranged at equal intervals around the circumference of a circle; with application of the results to the theory of atomic structure," *The London, Edinburgh,* and Dublin Philosophical Magazine and Journal of Science, vol. 7, no. 39, pp. 237–265, 1904.

[21] A. J. Petruska, J. B. Brink, and J. J. Abbott, "First demonstration of a modular and reconfigurable magnetic-manipulation system," in *Proc.*

IEEE Int. Conf. Robotics and Automation, 2015, pp. 149–155.